Journal of Materials Science: Materials in Electronics (2020) 31:17075–17083
https://doi.org/10.1007/s10854-020-04268-9

Gamma-irradiation synthesis of Fe_3O_4/rGO nanocomposites as lithium-ion battery anodes

Ying Liang[1] · **Wangli Lu**[1]

Received: 24 November 2019 / Accepted: 17 August 2020 / Published online: 27 August 2020

Abstract

Fe_3O_4/reduced graphene oxide (Fe_3O_4/rGO) nanocomposites with different weight concentration of Fe_3O_4 have been synthesized by a gamma-irradiation method. The iron(III) hydroxide and graphene oxide (GO) were reduced to Fe_3O_4 and rGO by the reducing species generated from the radiolysis of solvent. The Fe_3O_4 nanoparticles were anchored on the rGO nanosheets. The electrochemical performances of the obtained materials were evaluated in coin-type cells. As Li-ion rechargeable battery anodes, the discharge/charge cycling stability of Fe_3O_4/rGO composites is significantly improved in comparison with that of bare Fe_3O_4 nanoparticles. Among the studied composites, Fe_3O_4/rGO-2 (wt% of $Fe_3O_4 \approx 78.8\%$) shows the best cycling stability at a current density of 50 mA g^{-1}. The discharge capacity of Fe_3O_4/rGO-2 remains 568.6 mAh g^{-1} after 100 cycles. However, Fe_3O_4/rGO-3 (wt% of $Fe_3O_4 \approx 74.7\%$) exhibits an excellent cycling stability at a higher current density (500 mA g^{-1}), that the sustained discharge capacity is 738.5 mAh g^{-1} after 100 cycles.

1 Introduction

Transitional-metal oxides such as Fe_3O_4, Fe_2O_3, MnO_2, NiO, and Co_3O_4 have been considered as potential candidates for Li-ion battery anodes due to their high theoretical capacity. Among them, Fe_3O_4 has attracted much attention not only because of its high theoretical capacity (922 mAh g^{-1}), but also relating to its safety, high abundance, low cost, and environmental benignity [1–4]. However, large electrochemical polarization of Fe_3O_4 during lithiation/delithiation process causes the fast capacity fade. This defect inevitably hampers its practical use in Li-ion batteries [5].

Nanostructuring is generally considered to be an active way to enhance the electrochemical reaction dynamics of metal oxide materials by shortening the electrons and lithium-ion diffusion paths, while the nanosized materials always suffer from intrinsically prone to aggregation resulting in poor cycling performance [6–8]. To improve the cycling stability of Fe_3O_4 nanomaterials, combining it with graphene is recently deemed to be an effective strategy. Graphene possesses large specific surface area, good flexibility, extraordinary electrical property, and chemical stability [9–12]. Graphene oxide (GO), a derivative of graphene, has aroused great interest as the original support for anode materials during the chemical synthesis. The rich chemical structure on the surface of GO makes it compatible with a variety of materials to form composites. In the process of recombination with other substances, GO can be partially reduced to form reduced graphene oxide (rGO). In addition to having a large specific surface area and flexibility, the good electrical conductivity of graphene is partially retained in rGO. Therefore, extensive studies have been focused on the synthesis of Fe_3O_4/rGO composites such as co-precipitation method, solvothermal method, sonochemical precipitation, high-temperature reduction reaction, electrophoretic deposition route, thermal evaporation-induced method, and microwave-assisted combustion [13–19]. Herein, gamma irradiation as an environmentally friendly technique was successfully applied for the synthesis of Fe_3O_4/rGO composites at ambient temperature. Fe_3O_4/rGO composites as anode materials demonstrate high capacity and improved cycling performance. The characteristic properties and electrochemical performances of the obtained materials have been investigated and studied.

✉ Ying Liang
yliang@ecust.edu.cn

[1] Institute of Nuclear Technology and Application, School of Science, East China University of Science and Technology, Shanghai 200237, PR China

2 Experimental

2.1 Synthesis

Graphene oxide was firstly synthesized from natural graphite flakes by a modified Hummers method [20]. Then, aqueous suspension of GO at a concentration of 4.3 mg mL^{-1} was prepared. Fe_3O_4 and Fe_3O_4/rGO composites were synthesized by the gamma-irradiation method using $FeCl_3{\cdot}6H_2O$ and GO as the raw materials. In a typical procedure, 0.1081 g $FeCl_3{\cdot}6H_2O$ was dissolved in 40 mL deionized water. 0.04 g NaOH was added to form iron(III) hydroxide sol. Subsequently, GO aqueous solution containing a certain amount of GO (3.1 mg, 6.2 mg, 9.2 mg, and 12.4 mg, respectively) was dropped into the iron(III) hydroxide sol, followed by 10 mL isopropanol alcohol. Then the mixture was magnetic stirred for 30 min to get a homogeneous suspension and bubbled with pure Ar gas for 20 min to remove oxygen. After that, the suspension was exposed to gamma irradiation using a ^{60}Co source with a dose rate of ca. 170 Gy min^{-1}. After exposed for 15 h, the obtained black products were collected by centrifugation, washed with deionized water and absolute ethanol, and then dried at room temperature in a vacuum oven. Depending on the nominal amount of GO, the obtained materials were designated as Fe_3O_4/rGO-1, Fe_3O_4/rGO-2, Fe_3O_4/rGO-3, and Fe_3O_4/rGO-4, respectively. For comparison, black bare Fe_3O_4 nanoparticles were synthesized under the same conditions as Fe_3O_4/rGO composites.

2.2 Characterization

Powder X-ray diffraction (XRD) patterns were collected on an D/MAX-2550 diffractometer using Cu*K*α radiation over $5° \leq 2\theta \leq 80°$ with a step size of $\Delta 2\theta = 0.02°$. Raman spectra were performed on an Invia Reflex Raman Spectrometer at a wavelength of 514.5 nm. Thermogravimetric analysis (TGA) was carried out on a Netzsch STA 409PC instrument at a heating rate of 10 K/min from room temperature to 800 °C in an atmosphere of air. Fourier transform infrared spectra (FTIR) were taken by the KBr method on a Nicolet 6700 instrument in the range of 400–4000 cm^{-1}. The measurements of field-emission scanning electron microscope (FESEM) were conducted using a Hitachi S-4800 microscope. The measurements of X-ray photoelectron spectroscopy (XPS) were performed on an ESCALAB 250Xi spectrometer using Al*K*α radiation.

2.3 Electrode preparation and electrochemical characterization

The electrochemical experiments of the Fe_3O_4/rGO composites and bare Fe_3O_4 nanoparticles were tested using coin-type half-cells (CR2016) with Li foil as counter electrode. The working electrode was fabricated by mixing active powders, conductive acetylene black, and polyvinylidene fluoride binder dissolved in *n*-methyl pyrrolidinone with a weight ratio of 8:1:1 to form homogeneity slurry. The slurry was painted onto copper foil and dried at 85 °C under vacuum. Then, the copper foil with active material loading density of ca. ~ 1.0 mg cm^{-2} was punched into a disc. Coin-type half-cells (2016) were assembled in an Ar-filled glove box ($H_2O < 0.1$ ppm, $O_2 < 0.1$ ppm). The Celgard 2325 was used as the separator, a non-aqueous solution of $LiPF_6$ (1 M) in a 1:1:1 of ethylene carbonate (EC), diethyl carbonate (DEC), and dimethyl carbonate (DMC) as the electrolyte. The discharge/charge tests were performed in the voltage range of 0.01–3.0 V on a LANHE CT2001A battery test system. Cyclic voltammetry (CV) curves were measured at a scan rate of 0.1 mV s^{-1} within the range of 0.01–3.0 V (vs. Li/Li^+) using an electrochemistry working station (CHI618D).

3 Results and discussion

3.1 Phase composition

The radiolysis of water by gamma irradiation generates free radicals such as e_{aq}^-, H•, OH•, H_2, H_2O_2, and H_3O^+. It has been reported that hydrated electron (e_{aq}^-) and hydrogen radical (H•) are reducing species, while OH• and H_2O_2 are oxidizing species. e_{aq}^- are strong reducing agents which can reduce Fe (III) into Fe (II) [21–24]. The oxidizing radicals were scavenged by isopropanol alcohol during irradiation.

Figure 1 shows the XRD patterns of as-synthesized GO, bare Fe_3O_4, and Fe_3O_4/rGO composites. The XRD pattern of GO has a characteristic diffraction peak at $2\theta = 8.7°$ with a basal spacing of 1.0 nm. For bare Fe_3O_4 and Fe_3O_4/rGO composites, the diffraction peaks located at $2\theta = 30.2°$, 35.5°, 37.2°, 43.2°, 53.7°, 57.2°, 62.8°, 71.3°, and 74.3° can be assigned to the (220), (311), (222), (400), (422), (511), (440), (620), and (533) planes of cubic Fe_3O_4 (JCPDS file No. 19-0629), respectively. However, with the increase of rGO content in the composites, diffraction peaks of some other byproducts are observed in addition to the main Fe_3O_4 phase. Figure 2 shows the FTIR spectra of GO, bare Fe_3O_4, and Fe_3O_4/rGO composites. For GO, the

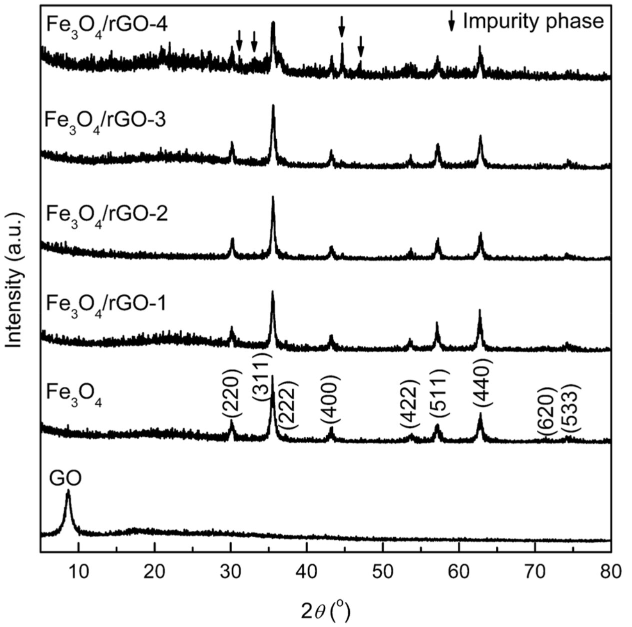

Fig. 1 XRD patterns of GO sheets, bare Fe_3O_4, Fe_3O_4/rGO-1, Fe_3O_4/rGO-2, Fe_3O_4/rGO-3, and Fe_3O_4/rGO-4 composites

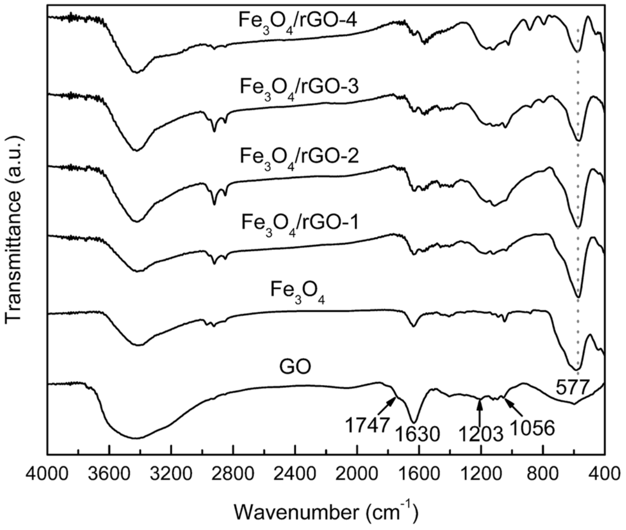

Fig. 2 FTIR spectra of GO sheets, bare Fe_3O_4, Fe_3O_4/rGO-1, Fe_3O_4/rGO-2, Fe_3O_4/rGO-3, and Fe_3O_4/rGO-4 composites

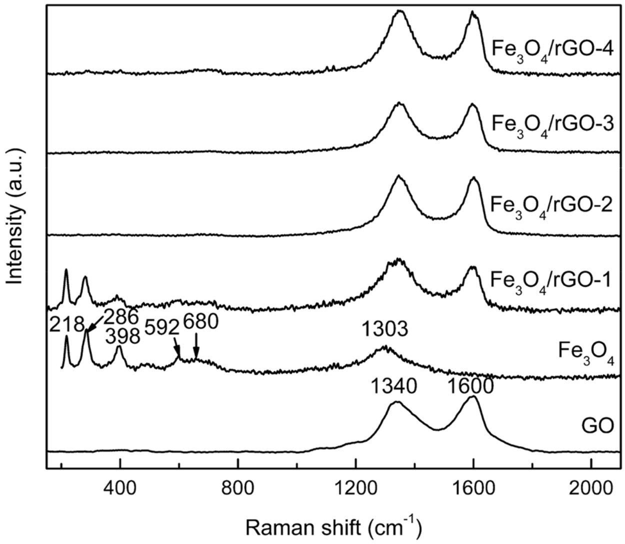

Fig. 3 Raman spectra of GO sheets, bare Fe_3O_4, Fe_3O_4/rGO-1, Fe_3O_4/rGO-2, Fe_3O_4/rGO-3, and Fe_3O_4/rGO-4 composites

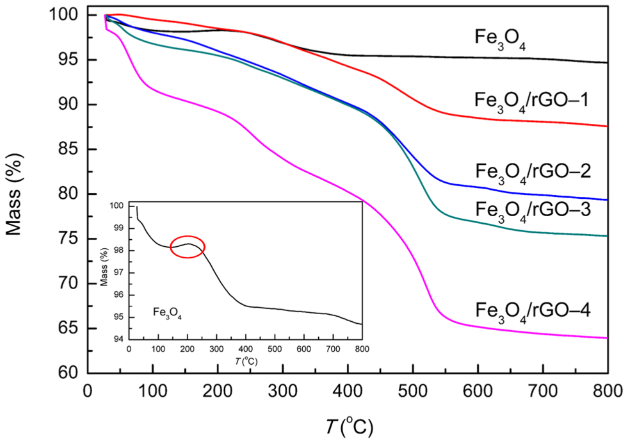

Fig. 4 TGA curves of bare Fe_3O_4, Fe_3O_4/rGO-1, Fe_3O_4/rGO-2, Fe_3O_4/rGO-3, and Fe_3O_4/rGO-4 composites

broadband around 3600–3200 cm^{-1} is attributed to the OH stretching vibration. The peak at 1630 cm^{-1} corresponds to the OH bending vibration. The two signals indicating the existence of adsorbed water molecules and structural OH groups can also be observed in the bare Fe_3O_4 and Fe_3O_4/rGO composites. The signal at 1747 cm^{-1} may be related to the C=O stretching vibrations of COOH groups situated at the edges of the GO sheets [25]. The peaks at 1203 cm^{-1} and 1056 cm^{-1} possibly arise from the epoxy and alkoxy C–O stretching, respectively [26]. For bare Fe_3O_4 and Fe_3O_4/rGO composites, the FTIR signals of some oxygen-containing functional groups (C=O and epoxy) are weakened, while the characteristic absorption peak at 577 cm^{-1} attributed to the Fe–O bond is observed [27]. To further explore the phase composition of the synthesized materials, Raman spectroscopic analysis was employed. As shown in Fig. 3, two typical peaks at 1340 cm^{-1} and 1600 cm^{-1} attributed to D and G bands of graphene are observed in the Raman spectra of GO and Fe_3O_4/rGO composites. For bare Fe_3O_4, the small broad signal centered at 680 cm^{-1} reveals the A_{1g} mode of Fe_3O_4 phase [28]. In addition, the peaks at 218 cm^{-1}, 286 cm^{-1}, 398 cm^{-1}, 592 cm^{-1}, and 1303 cm^{-1} can be attributed to the decomposition of Fe_3O_4 for Fe_2O_3 by the strong laser light used in Raman spectroscopic measurements [29]. However, the Raman signal of Fe_3O_4 in the Fe_3O_4/rGO composites is too weak to be clearly identified.

To quantify the weight percentage of Fe_3O_4 in the Fe_3O_4/rGO composites, TGA was carried out in air from room temperature to 800 °C. Figure 4 exhibits a small weight loss below 140 °C for bare Fe_3O_4 which is attributed to the evaporation of the adsorbed moisture. The weight increase between 140 and 210 °C clearly shown in the inset of Fig. 4 can be assigned to the oxidation of Fe_3O_4 to Fe_2O_3. This result further indicates that the product from gamma irradiation is Fe_3O_4 rather than Fe_2O_3. For the Fe_3O_4/rGO composites, there are three main weight loss processes. A slight weight loss below 200 °C is ascribed to the evaporation of the adsorbed moisture or gas molecules. Then the weight loss between 200 and 450 °C can be assigned to the destruction of labile oxygen-containing functional groups. The sharp weight loss in the step of 450–550 °C is due to the decomposition of rGO [30, 31]. From 550 to 800 °C, the weight of the samples remains and almost no loss occurs. Since the TGA process involves the oxidation of Fe_3O_4 to Fe_2O_3, the original weight percentage of Fe_3O_4 estimated from the remaining weight of Fe_2O_3 is to be 87.2%, 78.8%, 74.7%, and 63.2% for Fe_3O_4/rGO-1, Fe_3O_4/rGO-2, Fe_3O_4/rGO-3, and Fe_3O_4/rGO-4 composites, respectively. For Fe_3O_4/rGO-4 sample, the effect of impurities is ignored for the estimation of Fe_3O_4 weight percentage.

3.2 XPS study

To study the valence states of elements, XPS analyses were performed on the synthesized samples. In the survey spectra of Fig. 5a, two main peaks presented C 1s and O 1s are observed in the GO sheets. For bare Fe_3O_4 and Fe_3O_4/rGO composites, C 1s, O 1s and Fe 2p, Fe 3s, Fe 3p signals are evidently observed. The presence of C in bare Fe_3O_4 is caused by the adventitious carbon-based contaminant. The binding energy of C 1s peak at 284.6 eV is used as a reference for calibration for all the samples. Figure 5b shows the high-resolution Fe 2p XPS spectra of Fe_3O_4 and Fe_3O_4/rGO composites. The spectra can be split into Fe $2p_{3/2}$ and Fe $2p_{1/2}$ peaks. The peaks at 710.2 eV and 723.7 eV correspond to Fe^{2+} from FeO, and the peaks at 712.3 eV and 725.5 eV correspond to Fe^{3+} from Fe_2O_3 [32]. Weak satellite peaks are also observed at the bonding energy of 718.3 eV and 732.4 eV which can be attributed to the presence of Fe(III) symbiosis with Fe_3O_4. Furthermore, Fig. 5c displays the high-resolution O 1 *s* XPS spectra of GO, Fe_3O_4, and Fe_3O_4/rGO composites. The O 1s spectrum of GO is deconvoluted into three peaks at 531.3 eV, 532.5 eV, and 533.3 eV corresponding to the C=O, C−O−C, and C−OH groups, respectively. For bare Fe_3O_4, the peak at 529.9 eV is a typical state of Fe−O species, while the other peak at 531.1 eV is contributed by the adsorbed oxygen-containing groups in the sample. However, the O 1s spectra of the Fe_3O_4/rGO composites show three signals at 530.2 eV, 531.5 eV, and 533.0 eV which are attributed to the Fe−O, Fe−O−C, and C−OH groups, respectively [33]. The C 1s spectra of bare Fe_3O_4 and Fe_3O_4/rGO composites (Fig. 5d) are mainly composed of the C−C at 284.6 eV, C−O at 285.8 eV, and C=O at 288.4 eV [34]. Comparing with GO nanosheets, the intensity of carbon–oxygen bonding energy of Fe_3O_4/rGO composites remarkably decreases indicating the effective deoxygenation of GO under gamma irradiation.

3.3 Morphology

Figure 6 shows the TEM image of original GO sheets, SEM images of bare Fe_3O_4 sample, and Fe_3O_4/rGO composites. It is clearly observed in Fig. 6a that the GO nanosheets are ultrathin lamellar structure with wrinkles and folding on the surfaces. Figure 6b presents the morphology of bare Fe_3O_4 sample. It can be seen that the Fe_3O_4 nanoparticles with an approximate size of 30 nm are aggregated to larger particles, which would lead to the poor cycling performance as lithium-ion battery anodes. The SEM images (Fig. 6c–f) of Fe_3O_4/rGO composites illustrate that the rGO nanosheets are distributed between the loosely packed Fe_3O_4 nanoparticles which can prevent the aggregation of Fe_3O_4 particles to a certain extent.

3.4 Electrochemical performance

The electrochemical performances of Fe_3O_4 and Fe_3O_4/rGO composites were evaluated. Figure 7a–e shows the cyclic voltammetry (CV) curves for the first five cycles at a scan rate of 0.1 mV s^{-1}. The main cathodic peak in the first cycle is observed at about 0.61 V, 0.60 V, 0.59 V, 0.50 V, and 0.68 V for bare Fe_3O_4, Fe_3O_4/rGO-1, Fe_3O_4/rGO-2, Fe_3O_4/rGO-3, and Fe_3O_4/rGO-4, respectively, which represents the step-wise reduction of Fe^{3+} and Fe^{2+} to Fe^0 with the formation of Li_2O. The additional weak peaks around 1.55 V and 0.93 V can be associated with the irreversible reaction with the electrolyte to form a solid electrolyte interphase (SEI) film and insertion of Li^+ to form $Li_xFe_3O_4$. Meanwhile, the two anodic peaks at approximately 1.65 V and 1.84 V correspond to the reversible oxidation from Fe^0 to Fe^{2+} and Fe^{3+} [35]. In the second cycle, the main cathodic peak is positively shifted to high voltage at 0.72 V, 0.75 V, 0.81 V, 0.79 V, and 0.75 V for bare Fe_3O_4, Fe_3O_4/rGO-1, Fe_3O_4/rGO-2, Fe_3O_4/rGO-3, and Fe_3O_4/rGO-4, respectively, and the anodic peaks also shift to high voltage but not apparently as the cathodic peak. Moreover, for bare Fe_3O_4, the intensity of both cathodic and anodic peaks obviously decreases after the first cycle, which reveals the occurrence of irreversible

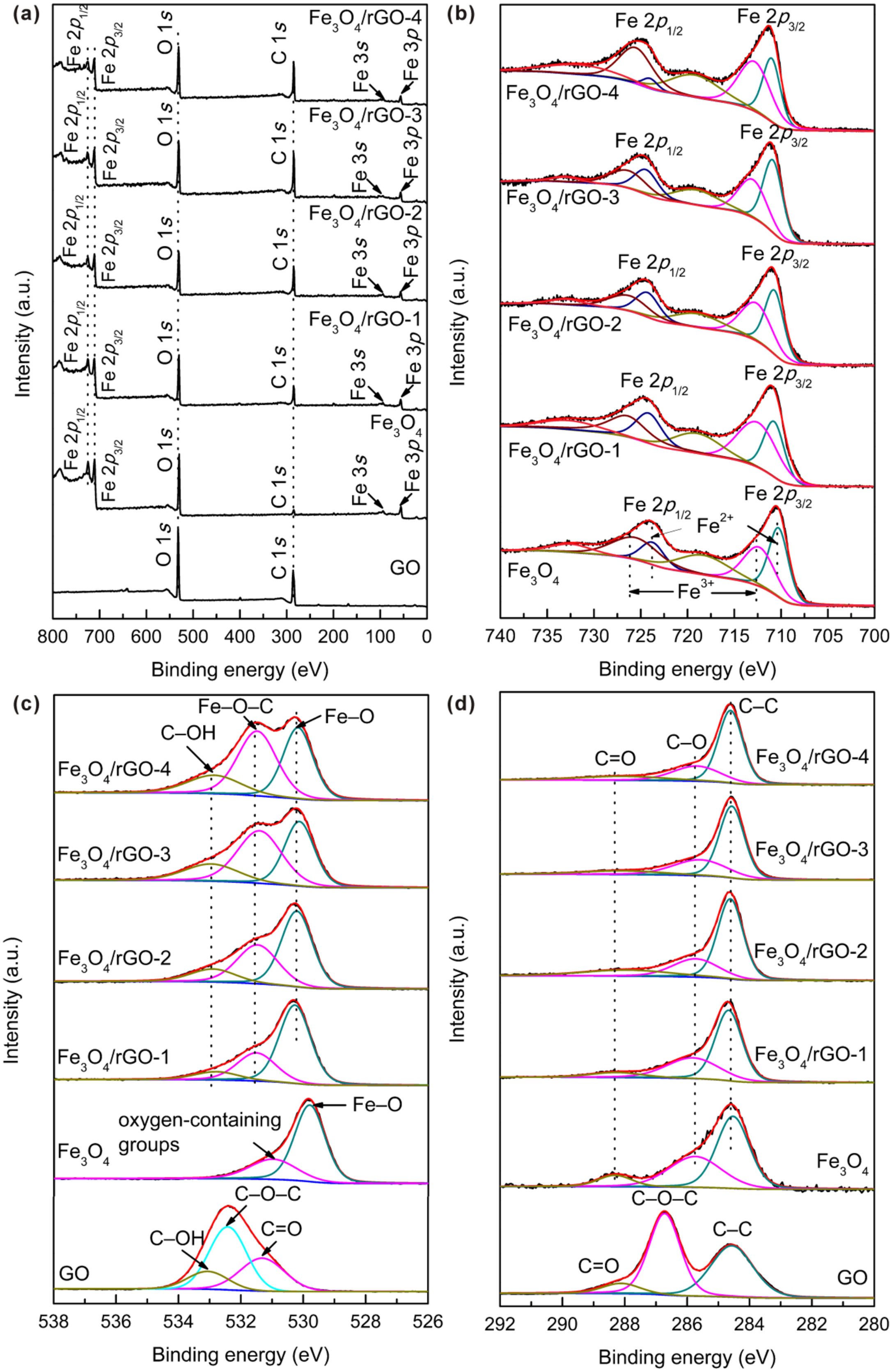

Fig. 5 XPS spectra of GO sheets, bare Fe_3O_4, Fe_3O_4/rGO-1, Fe_3O_4/rGO-2, Fe_3O_4/rGO-3, and Fe_3O_4/rGO-4 composites. **a** Survey spectrum, **b** XPS high-resolution spectra of the Fe 2p region, **c** O 1s region, and **d** C1s region

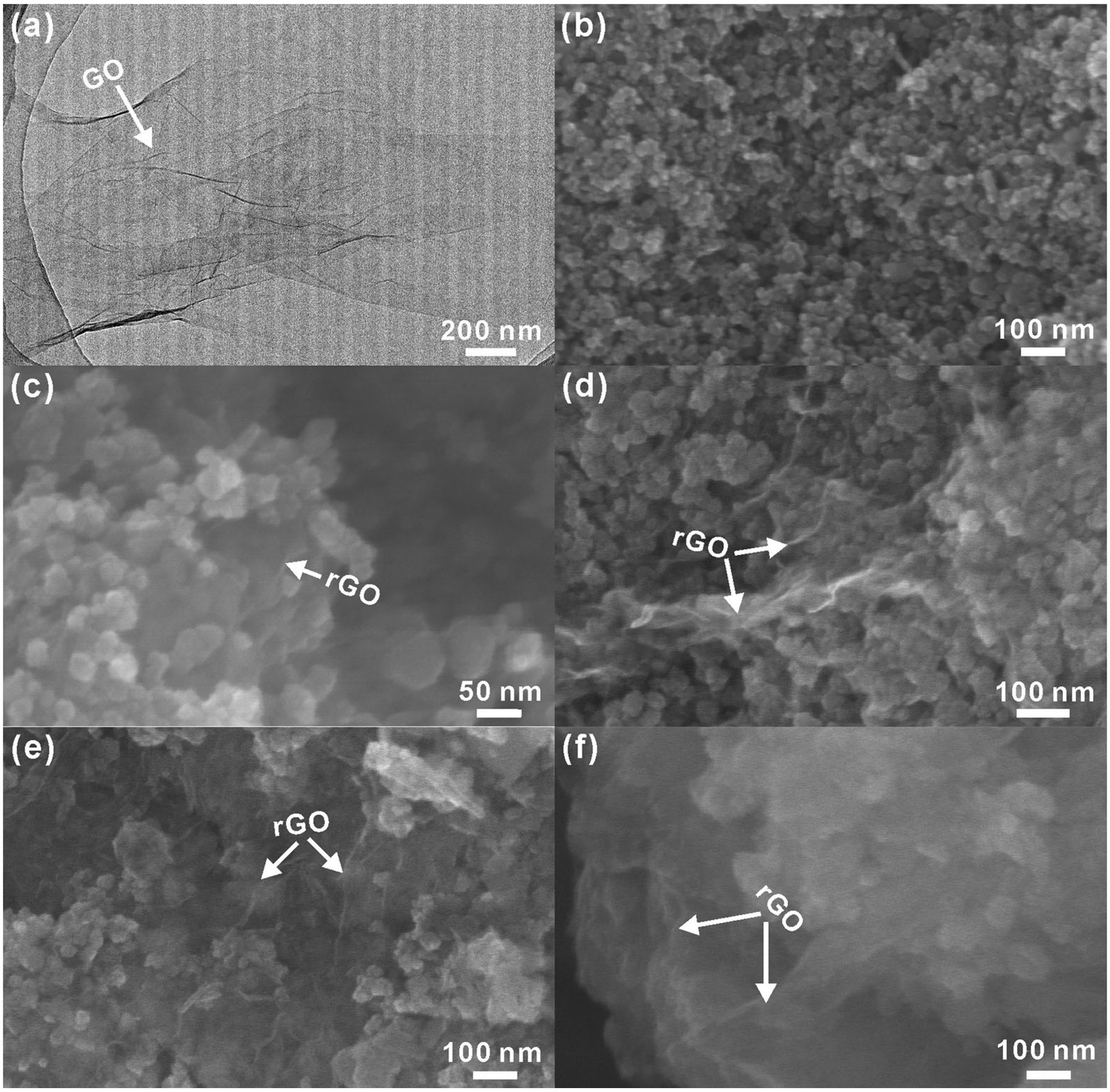

Fig. 6 **a** TEM image of GO sheets, and SEM images of **b** bare Fe_3O_4, **c** Fe_3O_4/rGO-1, **d** Fe_3O_4/rGO-2, **e** Fe_3O_4/rGO-3, and **f** Fe_3O_4/rGO-4 composites

reactions. Compared with bare Fe_3O_4, the changes of peak intensity and integrated areas for both cathodic and anodic peaks of Fe_3O_4/rGO composites are very limited from second to fifth cycle. The results indicate that the electrochemical reversibility of Fe_3O_4/rGO gradually builds after the initial cycle and is much better than that of bare Fe_3O_4.

For further analysis, Fig. 7f shows the galvanostatic discharge/charge performances of Fe_3O_4/rGO-2 composite for the 1st, 2nd, 3rd, 50th, and 100th cycles at a current density of 50 mA g^{-1} in the voltage range of 0.01−3.0 V. In the first discharge curve, there is a long potential plateau at ~ 0.81 V corresponding to the reduction of Fe^{3+}/Fe^{2+} to Fe^0. Short plateaus observed at ~ 1.64 V and ~ 1.08 V can be attributed to the lithium insertion. The following sloping region may be ascribed to the formation of a SEI film resulting in irreversible capacity loss. The sloping plateau at 1.50–2.10 V observed in the charging processes is due to the oxidation of Fe^0. The subsequent cycles of discharging process show the extended potential plateau at ~ 1.00 V. The potential plateau during charging process is not obviously changed. It can be found that almost all of the plateaus are corresponding to the peaks of CV curves.

Figure 8a presents the curves of the discharge/charge capacity versus the cycle number for the bare Fe_3O_4 nanoparticles and Fe_3O_4/rGO composites at the current density of 50 mA g^{-1}. Though, the bare Fe_3O_4 shows large first discharge/charge capacity with 1936.8/1467.9 mAh g^{-1}, fast capacity fading is observed in the subsequent cycles. The capacity of bare Fe_3O_4 remains 103.7/102.6 mAh g^{-1} and 120.3/118.6 mAh g^{-1} after 50 and 100 cycles, respectively.

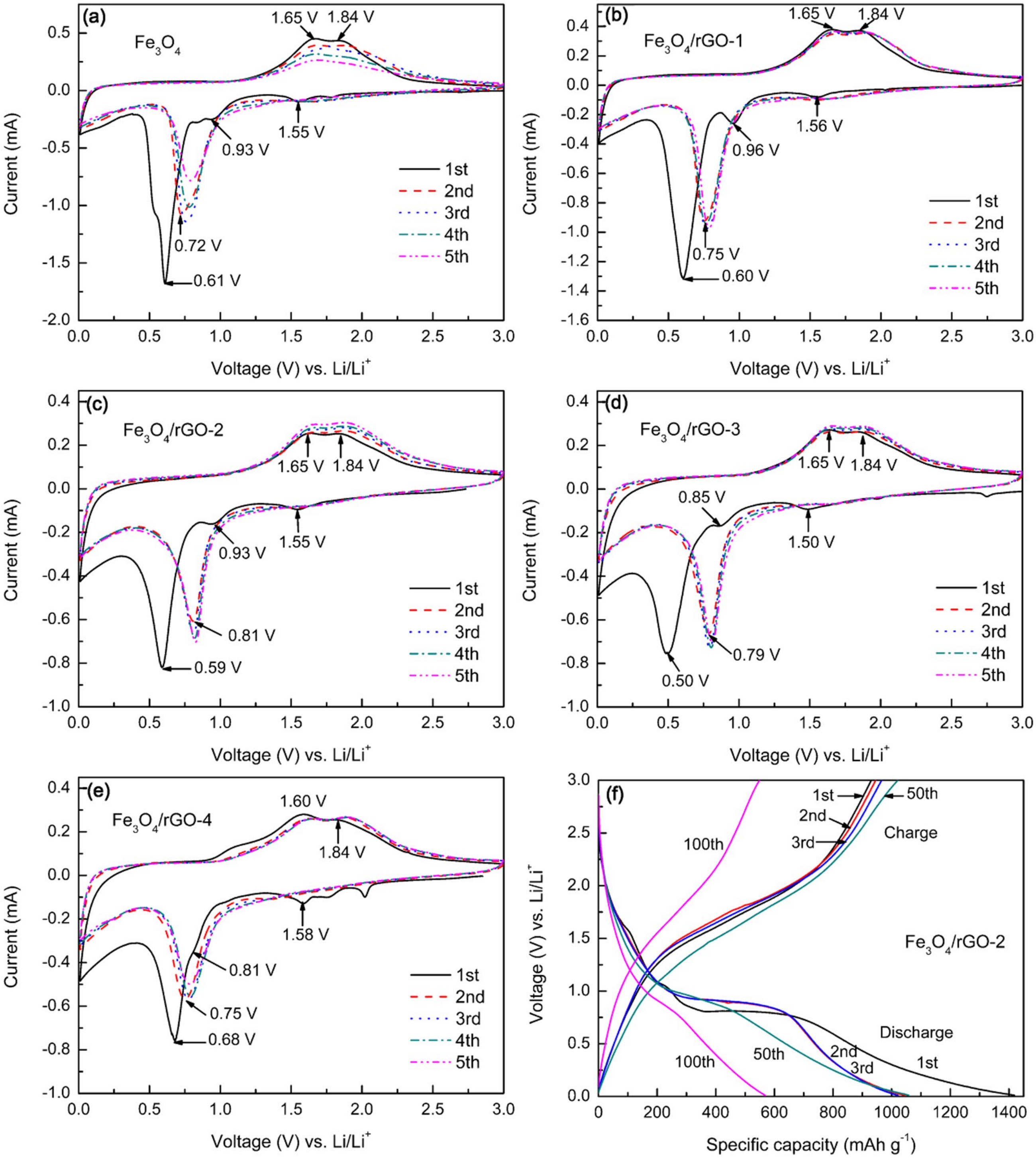

Fig. 7 Cyclic voltammograms of the **a** bare Fe_3O_4, **b** Fe_3O_4/rGO-1, **c** Fe_3O_4/rGO-2, **d** Fe_3O_4/rGO-3, and **e** Fe_3O_4/rGO-4 composites. **f** The 1st, 2nd, 3nd, 50th, and 100th galvanostatic discharge/charge profiles of Fe_3O_4/rGO-2 composite

For Fe_3O_4/rGO-1, Fe_3O_4/rGO-2, Fe_3O_4/rGO-3, and Fe_3O_4/rGO-4 composites, their first discharge/charge capacity with 1604.6/1187.2 mAh g^{-1}, 1418.8/947.2 mAh g^{-1}, 1799.8/1133.7 mAh g^{-1}, and 1579.8/967.9 mAh g^{-1} is lower than that of bare Fe_3O_4. However, the Fe_3O_4/rGO composites exhibit stable reversible capacity compared to bare Fe_3O_4 nanoparticles. For Fe_3O_4/rGO-1, the capacity is stable in initial 30 cycles and then rapidly decays from 1355.2/1318.3 mAh g^{-1} (30th cycle) to 257.7/260.2 mAh g^{-1} (50th cycle) and further 197.4/197.0 mAh g^{-1} (100th

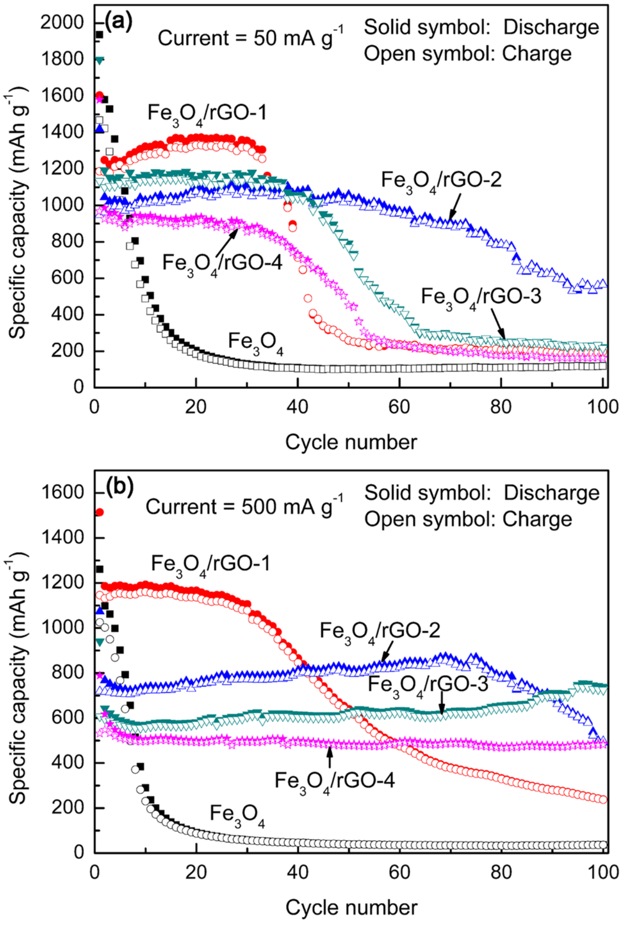

Fig. 8 Cycling performance of bare Fe$_3$O$_4$, Fe$_3$O$_4$/rGO-1, Fe$_3$O$_4$/rGO-2, Fe$_3$O$_4$/rGO-3, and Fe$_3$O$_4$/rGO-4 composites at the current density of **a** 50 mA g^{-1} and **b** 500 mA g^{-1}

Table 1 The retention of discharge capacity for bare Fe$_3$O$_4$, Fe$_3$O$_4$/rGO-1, Fe$_3$O$_4$/rGO-2, Fe$_3$O$_4$/rGO-3, and Fe$_3$O$_4$/rGO-4 composites after 100 cycles at different current densities

Sample	Fe$_3$O$_4$ concentration (%)	Capacity retention at 50 mA g^{-1} (%)	Capacity retention at 500 mA g^{-1} (%)
Fe$_3$O$_4$	100	6.2	2.9
Fe$_3$O$_4$/rGO-1	87.2	12.3	15.8
Fe$_3$O$_4$/rGO-2	78.8	40.1	45.7
Fe$_3$O$_4$/rGO-3	74.7	12.3	78.5
Fe$_3$O$_4$/rGO-4	63.2	10.4	61.6

cycle). The cycling performance of Fe$_3$O$_4$/rGO-2 is much superior to Fe$_3$O$_4$/rGO-1. Starting from the second cycle, the reversible discharge/charge specific capacity of Fe$_3$O$_4$/rGO-2 slightly increases to 1058.6/1037.1 mAh g^{-1} after 50 cycles and then gradually decreases to 568.6/565.5 mAh g^{-1} after 100 cycles. However, the cycling stability is not further improved with the increase of rGO concentration in the composites. For Fe$_3$O$_4$/rGO-3, the capacity is stable in the first forty cycles, then fast fades from 1013.6/1019.3 mAh g^{-1} (44th cycle) to 298.5/304.7 mAh g^{-1} (64th cycle) and further gradually decays to 221.8/216.1 mAh g^{-1} after the 100th cycle. And for Fe$_3$O$_4$/rGO-4, the sudden capacity degradation happens after the 34th cycle. Its discharge/charge capacity rapidly decreases from 850.6/835.7 mAh g^{-1} (34th cycle) to 274.7/274.4 mAh g^{-1} (55th cycle), and gradually decreases to 164.7/163.1 mAh g^{-1} after the 100th cycle. The results indicate that the existence of rGO sheets causes the decay of initial capacity in Fe$_3$O$_4$/rGO composites due to the much lower theoretical capacity of rGO than Fe$_3$O$_4$. Moreover, more defects on the surface and edge of rGO sheets can promote the formation of SEI film, which is an irreversible process, resulting in the low first coulombic efficiency. In addition, with the increase of rGO concentration, from Fe$_3$O$_4$/rGO-2 to Fe$_3$O$_4$/rGO-3 and Fe$_3$O$_4$/rGO-4, the cyclic stability becomes poor. In order to study the influence of current density on the stability of electrodes, higher current density was also applied for the test as shown in Fig. 8b. At the current density of 500 mA g^{-1}, a rapid decay of capacity is happened after the initial cycle for bare Fe$_3$O$_4$, while the capacity of Fe$_3$O$_4$/rGO-1 is stable from the second cycle to 20th cycle and then fast decays. For Fe$_3$O$_4$/rGO-2, the high discharge/charge capacity retains 868.6/850.1 mAh g^{-1} after 75 cycles and then decreases. However, the capacity of both Fe$_3$O$_4$/rGO-3 and Fe$_3$O$_4$/rGO-4 composites is stable from second cycle to 100th cycle, and even displays a trend to further increase. After 100 cycles, the discharge/charge capacity is 738.5/724.9 mAh g^{-1} and 486.4/481.6 mAh g^{-1} for Fe$_3$O$_4$/rGO-3 and Fe$_3$O$_4$/rGO-4, respectively. The capacity retention of samples at different current densities is presented in Table 1. The cyclic stability of Fe$_3$O$_4$/rGO composites is significantly improved compared to bare Fe$_3$O$_4$ nanoparticles, because the rGO sheets can be a good matrix to prevent the volume expansion and particle aggregation of Fe$_3$O$_4$. The positive influence of rGO is significant at the high current density. However, due to the good compatibility between rGO and electrolyte, a lower current density can give enough time for some reactions to proceed. As a result, the SEI film becomes thicker in the composites with higher rGO concentration. The thick SEI film leads to a fast capacity fading. Therefore, Fe$_3$O$_4$/rGO-3 and Fe$_3$O$_4$/rGO-4 behave with much poor cycling performances than that of Fe$_3$O$_4$/rGO-2 at the current density of 50 mA g^{-1}.

4 Conclusions

In summary, gamma-irradiation method was demonstrated for the synthesis of bare Fe$_3$O$_4$ nanoparticles and its composites with rGO sheets. As anode electrodes for

Li-ion batteries, Fe_3O_4/rGO composites exhibit dramatically improved cycle stability than bare Fe_3O_4 electrode due to the acting of rGO sheets. In addition, the electrochemical performances of Fe_3O_4/rGO composites are closely related to the content of rGO. This study provides a facile environmental method to the synthesis of potential anode material candidates for the lithium-ion batteries.

Acknowledgements The authors thank Research Center of Analysis and Test of East China University of Science and Technology for the help on sample analysis.

References

1. T. Xia, X. Xu, J. Wang, C. Xu, F. Meng, Z. Shi, J. Lian, J.M. Bassat, Electrochim. Acta **160**, 114 (2015)
2. X. Wang, Y. Liu, H. Arandiyan, H. Yang, L. Bai, J. Mujtaba, Q. Wang, S. Liu, H. Sun, Appl. Surf. Sci. **389**, 240 (2016)
3. S.H. Lee, S.H. Yu, J.E. Lee, A. Jin, D.J. Lee, N. Lee, H. Jo, K. Shin, T.Y. Ahn, Y.W. Kim, H. Choe, Y.E. Sung, T. Hyeon, Nano Lett. **13**, 4249 (2013)
4. Y. Chen, H. Xia, L. Lu, J. Xue, J. Mater. Chem. **22**, 5006 (2012)
5. S. Mitra, P. Poizot, A. Finke, J.M. Tarascon, Adv. Funct. Mater. **16**, 2281 (2006)
6. P.G. Bruce, B. Scrosati, J.M. Tarascon, Angew. Chem. Int. Ed. **47**, 2930 (2008)
7. C. Li, Z. Li, X. Ye, X. Yang, G. Zhang, Z. Li, Chem. Eng. J. **334**, 1614 (2018)
8. K. Zhang, W. Zhao, J.T. Lee, G. Jang, X. Shi, J.H. Park, J. Mater. Chem. A **2**, 9636 (2014)
9. Y. Dong, K.C. Yung, R. Ma, X. Yang, Y.S. Chui, J.M. Lee, J.A. Zapien, Carbon **86**, 310 (2015)
10. M. Ren, M. Yang, W. Liu, M. Li, L. Su, C. Qiao, X. Wu, H. Ma, Electrochim. Acta **194**, 219 (2016)
11. S. Zhou, Y. Zhou, W. Jiang, H. Guo, Z. Wang, X. Li, Appl. Surf. Sci. **439**, 927 (2018)
12. L. Qi, Y. Xin, Z. Zuo, C. Yang, K. Wu, B. Wu, H. Zhou, A.C.S. Appl, Mater. Interfaces **8**, 17245 (2016)
13. C. Liang, T. Zhai, W. Wang, J. Chen, W. Zhao, X. Lu, Y. Tong, J. Mater. Chem. A **2**, 7214 (2014)
14. K. Zhu, Y. Zhang, H. Qiu, Y. Meng, Y. Gao, X. Meng, Z. Gao, G. Chen, Y. Wei, J. Alloys Compd. **675**, 399 (2016)
15. K. Wu, D. Liu, W. Lu, K. Zhang, Ultrason. Sonochem. **45**, 167 (2018)
16. L. Ji, Z. Tan, T.R. Kuykendall, S. Aloni, S. Xun, E. Lin, V. Battaglia, Y. Zhang, Phys. Chem. Chem. Phys. **13**, 7170 (2011)
17. Y. Yang, J. Li, D. Chen, J. Zhao, A.C.S. Appl, Mater. Interfaces **8**, 26730 (2016)
18. Y. Dong, R. Ma, M. Hu, H. Cheng, Q. Yang, Y.Y. Li, J.A. Zapien, Phys. Chem. Chem. Phys. **15**, 7174 (2013)
19. S. Bhuvaneswari, P.M. Pratheeksha, S. Anandan, D. Rangappa, R. Gopalan, T.N. Rao, Phys. Chem. Chem. Phys. **16**, 5284 (2014)
20. D.C. Marcano, D.V. Kosynkin, J.M. Berlin, A. Sinitskii, Z. Sun, A. Slesarev, L.B. Alemany, W. Lu, J.M. Tour, ACS Nano **4**, 4806 (2010)
21. B.G. Ekoko, R. Zhou, L. Xin, K.K. Lobo, L. Ilinga, J. Radioanal. Nucl. Chem. **270**, 473 (2006)
22. T. Jurkin, M. Gotić, G. Štefanić, I. Pucić, Radiat. Phys. Chem. **124**, 75 (2016)
23. A. Abedini, A.R. Daud, M.A.A. Hamid, N.K. Othman, PLoS ONE **9**, e90055 (2014)
24. S. Wang, H. Xin, Radiat. Phys. Chem. **56**, 567 (1999)
25. G. Shao, Y. Lu, F. Wu, C. Yang, F. Zeng, Q. Wu, J. Mater. Sci. **47**, 4400 (2012)
26. J. Pu, S. Wan, W. Zhao, Y. Mo, X. Zhang, L. Wang, Q. Xue, J. Phys. Chem. C **115**, 13275 (2011)
27. S.R. Kumar, J.G. Kim, C. Viswanathan, W.B. Kim, R.K. Selvan, N. Ponpandian, Mater. Res. Bull. **97**, 272 (2018)
28. X. Li, X. Zheng, J. Shao, T. Gao, Q. Shi, Q. Qu, Chem. Eur. J. **22**, 376 (2016)
29. M. Sathish, T. Tomai, I. Honma, J. Power Sources **217**, 85 (2012)
30. L. Qin, S. Liang, X. Tan, G. Yan, Electrochemistry **85**, 397 (2017)
31. Y. Chang, J. Li, B. Wang, H. Luo, L. Zhi, J. Mater. Sci. Technol. **30**, 759 (2014)
32. T. Fujii, F.M.F. de Groot, G.A. Sawatzky, F.C. Voogt, T. Hibma, K. Okada, Phys. Rev. B **59**, 3195 (1999)
33. S.M. Hao, Q.J. Li, J. Qu, F. An, Y.J. Zhang, Z.Z. Yu, A.C.S. Appl, Mater. Interfaces **10**, 17923 (2018)
34. S. Wang, D. Yu, L. Dai, D.W. Chang, J.B. Baek, ACS Nano **5**, 6202 (2011)
35. J.Z. Wang, C. Zhong, D. Wexler, N.H. Idris, Z.X. Wang, L.Q. Chen, H.K. Liu, Chem. Eur. J. **17**, 661 (2011)